AIP Advances

Investigation of carrier transport and collection characteristics for GaAs-based betavoltaic batteries

Cite as: AIP Advances **11**, 105108 (2021); https://doi.org/10.1063/5.0068261
Submitted: 24 August 2021 • Accepted: 23 September 2021 • Published Online: 07 October 2021

Renzhou Zheng, Yu Wang, Jingbin Lu, et al.

ARTICLES YOU MAY BE INTERESTED IN

Breaking the myth: Wide-bandgap semiconductors not always the best for betavoltaic batteries
Applied Physics Letters **119**, 153904 (2021); https://doi.org/10.1063/5.0068269

Theoretical study of a high-efficiency GaP–Si heterojunction betavoltaic cell compared with metal–Si Schottky barrier betavoltaic cell
AIP Advances **11**, 065110 (2021); https://doi.org/10.1063/5.0053917

High power direct energy conversion by nuclear batteries
Applied Physics Reviews **6**, 031305 (2019); https://doi.org/10.1063/1.5123163

Investigation of carrier transport and collection characteristics for GaAs-based betavoltaic batteries

Cite as: AIP Advances 11, 105108 (2021); doi: 10.1063/5.0068261
Submitted: 24 August 2021 • Accepted: 23 September 2021 •
Published Online: 7 October 2021

Renzhou Zheng,[1] **Yu Wang,**[1] **Jingbin Lu,**[1,a)] **Xiaoyi Li,**[1] **Ziyi Chen,**[1] **Xue Zhang,**[1] **Yuehui Zhang,**[1]
Yugang Zeng,[2] **Lei Liang,**[2,3] **Li Qin,**[2] **Yongyi Chen,**[2] **and Yumin Liu**[4]

AFFILIATIONS

[1] College of Physics, Jilin University, Changchun 130012, China
[2] State Key Laboratory of Luminescence and Applications, Changchun Institute of Optics, Fine Mechanics and Physics, Chinese Academy of Sciences, Changchun 130033, China
[3] Center of Materials Science and Optoelectronics Engineering, University of Chinese Academy of Sciences, Beijing 100049, China
[4] College of Nuclear Science and Engineering, East China University of Technology, Nanchang 330013, China

[a)] **Author to whom correspondence should be addressed:** ljb@jlu.edu.cn

ABSTRACT

This paper presents a simulation model to predict the performance of GaAs-based betavoltaic batteries with a p–n junction structure, in which the carrier transport and collection characteristics were studied. First, the electron–hole pair generation rate in the GaAs material under the irradiation of a ^{63}Ni source was calculated using the Monte Carlo codes. Furthermore, by simulating the energy band structure, electric field distribution, and current density distribution in batteries with the finite element analysis software COMSOL Multiphysics, we analyzed the effects of structure parameters on the output performance. Our simulation results showed that the short-circuit current density (J_{sc}), open-circuit voltage (V_{oc}), maximum output power density (P_m), and energy conversion efficiency (η) of the batteries are significantly affected by the thicknesses and doping concentrations of the p-region and n-region ($H_{\text{p-GaAs}}$, $H_{\text{n-GaAs}}$, N_a, and N_d). The optimized GaAs-based battery with an $H_{\text{p-GaAs}}$ value of 0.1 μm, an $H_{\text{n-GaAs}}$ value of 9.9 μm, an N_a value of 3.98×10^{16} cm^{-3}, and an N_d value of 1×10^{15} cm^{-3} can achieve a P_m value of 0.080 μW/cm^2. The related J_{sc}, V_{oc}, and η values are 0.234 μA/cm^2, 0.49 V, and 1.55%, respectively. When the top and bottom heavily doped layers are introduced, the P_m value of the battery is enhanced by 7.5% compared to that of the battery without heavily doped layers due to the formed drift fields.

I. INTRODUCTION

Betavoltaic batteries using radioactive isotopes emitting beta particles have been studied for powering the micro-devices due to their long service life, high power density, and strong environmental adaptability.[1,2] These batteries are composed of a semiconductor energy converter and a beta source, and their operational principle is similar to that of a photovoltaic battery. The beta particles interact with the semiconductors and create thousands of electron–hole pairs (EHPs) through impact ionization. Then, these EHPs can be collected in the energy converter through certain transport mechanisms, forming the radiation-induced current and converting the decay energy into electrical energy.

GaAs is a direct bandgap III–V compound semiconductor, which has the advantages of wide bandgap (1.424 eV), high electron mobility [~8000 cm^2/(V s)], and high threshold energy for radiation damage (270 keV).[3] Due to its low intrinsic carrier concentration, the GaAs-based betavoltaic batteries can have a low leakage current and a high open-circuit voltage. Additionally, the growth and processing techniques of GaAs are relatively mature, and it is easy to fabricate a high quality betavoltaic device.[4] These make GaAs an ideal energy conversion material for the betavoltaic batteries. In the past decade, the betavoltaic batteries with a p–n junction and Schottky barrier structures have been extensively studied.[5–10] The performances of these batteries were mainly investigated with the effects of structure parameters, such as doping concentrations and junction depth.[11–13] However, the experimental results of the fabricated batteries show very low energy conversion efficiency, and the performance prediction and optimization design are always unsatisfactory.[14–17] On the one hand, due to the self-absorption of the source, the apparent power density is much less than the total power density, resulting in the low utilization efficiency of the source and the small output power density of batteries. Fortunately, recent studies have shown that the transport process of beta particles in the energy conversion material can be well simulated by using the Monte Carlo codes, in which the self-absorption is considered.[18] Therefore, through certain simulation calculations, the geometry of the source can be optimized to improve the utilization efficiency of the source in a betavoltaic battery. The battery performance predictions considering the self-absorption of the source are more accurate. On the other hand, theoretical calculations on the output parameters are almost based on the analytical expressions, which are obtained by solving the minority carrier diffusion equation with a lot of hypotheses,[11,12,19] eventually resulting in an unreliable performance prediction and even structure design. Although using the energy deposition distribution of the source simulated by Monte Carlo codes and then using the Klein formula to calculate the EHP generation rate distribution are proved to be reasonable,[20] the transport and collection processes of carriers inside the battery cannot be described in detail, especially through the analytical expressions for calculating the radiation-induced current. Therefore, further investigations of carrier transport and collection characteristics are needed for improving the accuracy of performance prediction and structure design of the betavoltaic batteries.

Recent research studies have shown that it is feasible to investigate the performance of a betavoltaic battery using device simulators, such as Synopsys Medici, technology computer-aided design (TCAD), and COMSOL Multiphysics.[21–27] In 2016, the performance of a 4H–SiC betavoltaic battery was predicted using the Monte Carlo code and Synopsys Medici device simulator.[22] They investigated the effects of source thickness and the thickness and doping concentration of the p-region on the battery performance and proposed the optimal design. In 2020, a GaN-based betavoltaic battery with an AlGaN back-barrier layer was reported.[25] In this research, a three-dimensional (3D) TCAD simulator was used to optimize the finger structure, which can improve the output power density of the battery. In the same year, the betavoltaic generators based on the nanowire were presented, which are made of Si, GaAs, and GaP for ^{63}Ni and tritium sources.[26] The energy deposition distribution of beta particles was obtained by using the Monte Carlo simulations, and furthermore, the nanowire geometry was optimized. In addition, the current–voltage (I–V) characteristics and maximum power of the batteries were determined using COMSOL Multiphysics, and the optimal diode designs are suggested. According to these studies, the performance predictions of betavoltaic batteries by the device simulators are reliable and accurate. However, there is little discussion about the energy band structure and current density distribution inside the betavoltaic battery, which essentially determine the battery performance. It is necessary to take a detailed observation during the physical processes that take place inside the battery, especially carrier transport and collection characteristics. This can contribute to illuminating the effects of structure parameters on the battery performance, further guiding the optimization and fabrication.

In this paper, we presented a simulation model to predict the performance of GaAs-based betavoltaic batteries with a p–n junction structure, in which the carrier transport and collection characteristics were studied. The electron–hole pair generation rate in the GaAs material under the irradiation of a ^{63}Ni source was calculated by using the Monte Carlo codes. To accurately predict the performance of GaAs-based batteries, the finite element analysis software COMSOL Multiphysics was used to investigate the carrier transport and collection characteristics. The proposed GaAs-based batteries have four layers: a top heavily doped p^+-GaAs layer, a p-GaAs layer, an n-GaAs layer, and a bottom heavily doped n^+-GaAs layer. In order to enhance the carrier collection and optimize the structure parameters of the batteries, the effects of thicknesses and doping concentrations of the p-region and n-region on the output parameters were analyzed. Specifically, the energy band structure, electric field distribution, current density distribution, and current density–voltage characteristics of the batteries were obtained, and finally, the optimized output performances, including short-circuit current density, open-circuit voltage, and maximum output power density, were achieved. These results have guiding significance for the performance improvement, optimization design, and experimental preparation of the GaAs-based betavoltaic batteries. Our simulation model can be extended to the betavoltaic batteries with other semiconductors and radioactive isotopes.

II. DEVICE STRUCTURE AND SIMULATION METHOD

The simulation process consists of two parts: the simulation of energy deposition distribution of beta particles in the semiconductor energy converter and the simulation of electrical characteristics of devices. The energy deposition distribution of ^{63}Ni beta particles in the GaAs material is simulated by using the Monte Carlo codes, and furthermore, the electron–hole pair generation rate is obtained. The output performances of batteries are determined by using COMSOL Multiphysics in which the electron–hole pair generation rate from the Monte Carlo simulation is utilized as input.

A. Monte Carlo simulation and energy deposition distribution

In this study, a 2 μm-thick ^{63}Ni source (with a total activity density of 100 mCi/cm^2) is selected for the GaAs-based batteries with a p–n junction structure. The energy deposition distribution of beta particles in the GaAs material determines the spatial distribution of the electron-hole pair generation rate. In this part, a rectangular ^{63}Ni source (1 cm × 1 cm × 2 μm) with a full energy spectrum is used to calculate the energy deposition along the radiation transport depth in GaAs bulk ($1 \times 1 \times 0.5$ cm^3), and the prototype structure of the simulation model is shown in Fig. 1(a). Klein reported the average energy dissipated per electron-hole pair generated as $E_{ehp} = 2.8\ E_g + 0.5$ eV, where E_g is the bandgap of the semiconductor.[20] Furthermore, the electron–hole pair generation rate $[G(Y)]$ is obtained, and as shown in Fig. 1(b), it decreases exponentially with the increase in radiation transport depth (Y) and can be expressed using the following formula:

$$G(Y) = \frac{E(Y)}{E_{ehp}} = G_0 \exp(-\alpha Y), \qquad (1)$$

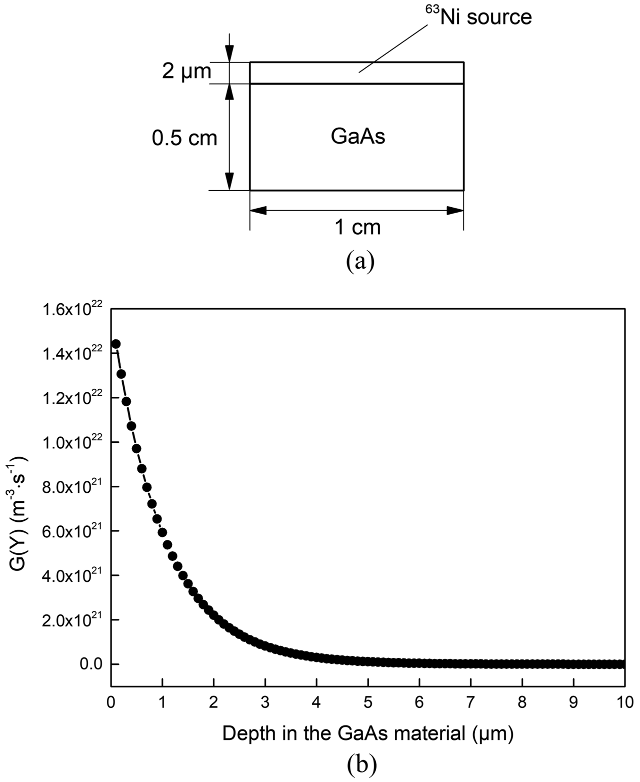

FIG. 1. (a) Prototype structure of the simulation model. (b) Electron–hole pair generation rate in the GaAs material vs radiation transport depth.

where $E(Y)$ is the energy deposition rate in the GaAs material and G_0 and α are the exponential fitting parameters ($G_0 = 1.5907 \times 10^{22}$ m^{-3} s^{-1} and $\alpha = 0.987\,67$ μm^{-1}).

B. Geometry, materials, and mesh

COMSOL Multiphysics is used to model the GaAs-based betavoltaic batteries with a p–n junction structure, which have four layers: the top p$^+$-GaAs and bottom n$^+$-GaAs layers are heavily doped for better metal contact, and the p-GaAs and n-GaAs layers in the middle are used to form the depletion region. As shown in Fig. 2(a), the overall dimension of the battery is 1 × 1 × 10 μm^3. Using 10 μm as the total thickness of the battery is based on the maximum radiation transport depth of ^{63}Ni beta particles in GaAs [Fig. 1(b)]. The thicknesses of the top p$^+$-GaAs and bottom n$^+$-GaAs layers are set to 0.1 μm. The thicknesses of the p-region and n-region ($H_{\text{p-GaAs}}$ and $H_{\text{n-GaAs}}$) are variables, and they will be optimized in the following simulations. The most material properties of GaAs are imported from the COMSOL library, but some properties, such as minority carrier mobility and minority carrier lifetime, are not available in the library, so we manually added them from the literature.[28,29] To improve the accuracy of results and to obtain a faster computation time, a user-controlled mesh is defined for the 2D geometry with a thickness of 1 μm, as shown in Fig. 2(b). The maximum and minimum element sizes are 10 and 1 nm, respectively. The maximum element growth rate is set to 1.08 with a curvature factor of 0.25, and the resolution of narrow regions is specified to be 1.

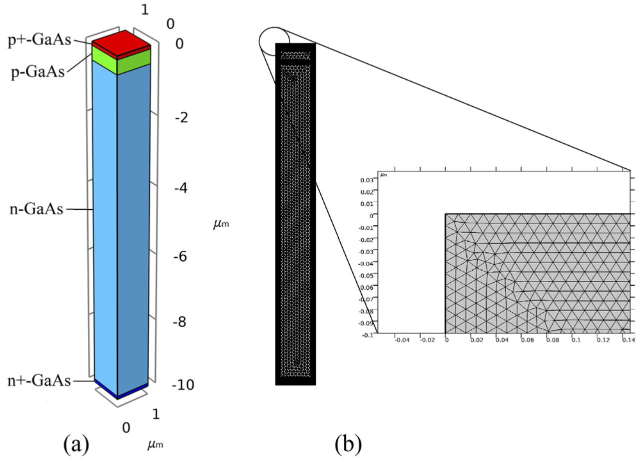

FIG. 2. (a) Schematic and geometry of the GaAs-based betavoltaic battery. (b) Meshed structure.

C. Physics

In this study, our focus is on the carrier transport and collection simulations; thus, the finite element method is used to solve the coupled Poisson and carrier continuity equations[30,31] as follows:

$$\nabla^2 V = -\frac{\rho}{\epsilon_0 \epsilon_r}, \tag{2}$$

$$-\frac{1}{q}\nabla j_n = G - R_n, \tag{3}$$

$$\frac{1}{q}\nabla j_p = G - R_p, \tag{4}$$

where V is the electrostatic potential, ρ is the charge density, ϵ_0 is the vacuum permittivity, ϵ_r is the relative permittivity of the material, q is the electron charge, G is the electron–hole pair generation rate, and R_n (R_p) is the electron (hole) recombination rate. j_n (j_p) is the electron (hole) current density, which can be expressed as[30]

$$j_n = -\frac{\mu_n kT}{q}\nabla n + \mu_n n \nabla V, \tag{5}$$

$$j_p = -\frac{\mu_p kT}{q}\nabla p - \mu_p p \nabla V, \tag{6}$$

where μ_n (μ_p) is the electron (hole) mobility, k is Boltzmann's constant, T is the absolute temperature, and n (p) is the electron (hole) concentration.

The battery is assumed to be operating at room temperature (300 K), and various physical models are employed in the simulations. First of all, the COMSOL calculations utilize the electron-hole pair generation rate from the Monte Carlo simulation as input. Second, the analytic doping model features are used to define the

TABLE I. Semiconductor properties of GaAs used in COMSOL Multiphysics.

	Parameter	Value
Relative permittivity	ϵ_r	12.9
Bandgap	E_g	1.424 eV
Electron affinity potential	χ	4.07 eV
Effective density of states in the conduction band	N_c	4.7×10^{17} cm^{-3}
Effective density of states in the valence band	N_v	7.0×10^{18} cm^{-3}
Minority electron mobility	μ_a	500 cm^2/(V s)
	μ_b	9400 cm^2/(V s)
	N_{ref}	6.0×10^{16} cm^{-3}
	d	0.394
Minority hole mobility	μ_a	20 cm^2/(V s)
	μ_b	491.5 cm^2/(V s)
	N_{ref}	1.48×10^{17} cm^{-3}
	d	0.38
Minority electron lifetime	τ_0	1×10^{-6} s
	N_{ref}	1.00×10^{16} cm^{-3}
Minority hole lifetime	τ_0	2×10^{-8} s
	N_{ref}	2.00×10^{18} cm^{-3}

background doping and the main p and n sections of the device. The geometric doping models are used to create highly doped layers at the top and bottom of the device. The low-field mobility model is used to calculate the minority carrier mobility, which is a function of doping concentration,[28]

$$\mu(N) = \mu_a + \frac{\mu_b - \mu_a}{1 + \left(\frac{N}{N_{ref}}\right)^d}, \tag{7}$$

where N is the net doping concentration and μ_a, μ_b, N_{ref}, and d are the fitting parameters that can be obtained from the literature.[28] In addition, the Shockley–Read–Hall (SRH) model is used to define the trap-assisted recombination, with associated parameters, such as low-injection minority carrier lifetime, which can be expressed as[29]

$$\tau(N) = \frac{\tau_0}{1 + \left(\frac{N}{N_{ref}}\right)}, \tag{8}$$

where τ_0 is the intrinsic lifetime. The semiconductor properties of GaAs used in COMSOL Multiphysics are listed in Table I.[28,29]

III. RESULTS AND DISCUSSION

To maximize the output power density and optimize the structure parameters of the GaAs-based betavoltaic batteries, the parametric sweep is used in the COMSOL model to tune the variables including the thicknesses of the p-region and n-region ($H_{\text{p-GaAs}}$ and $H_{\text{n-GaAs}}$), the acceptor concentration of the p-region (N_a), and the donor concentration of the n-region (N_d). The feasible $H_{\text{p-GaAs}}$ value ranged from 0.1 to 5 μm, $H_{\text{n-GaAs}}$ = 10 μm–$H_{\text{p-GaAs}}$, the feasible N_a value ranged from 1 $\times 10^{15}$ to 1 $\times 10^{18}$ cm^{-3}, and the feasible N_d value ranged from 1 $\times 10^{14}$ to 1 $\times 10^{15}$ cm^{-3}. In addition, the $H_{\text{p-GaAs}}$, $H_{\text{n-GaAs}}$, N_a, and N_d values of the structure as initial values are 0.5 μm, 9.5 μm, 1 $\times 10^{16}$ cm^{-3}, and 1 $\times 10^{15}$ cm^{-3}, respectively. The acceptor concentration and donor concentration of the heavily doped top p$^+$-GaAs and bottom n$^+$-GaAs layers (N_A and N_D) are set to 1 $\times 10^{18}$ and 1 $\times 10^{17}$ cm^{-3}, respectively.

A. Energy bands, electric field distribution, and carrier concentration

Figure 3(a) shows the energy diagram of the battery at thermodynamic equilibrium. For the battery without top and bottom heavily doped layers, the relative positions of the conduction and valence bands (E_c and E_v) between the p-region and n-region change with the position of the Fermi energy level (E_F), and as a result, the conduction band and valence band in the space charge region will be bent.[32] Meanwhile, an energy potential barrier (built-in potential barrier) of 1.04 eV is formed, and it blocks the electrons in the n-region from moving into the p-region and maintains the equilibrium of carrier diffusion and drift. When the top and bottom layers are heavily doped, the Fermi energy level in the p$^+$-GaAs layer is close to the valence band, and the Fermi energy level in the n$^+$-GaAs layer

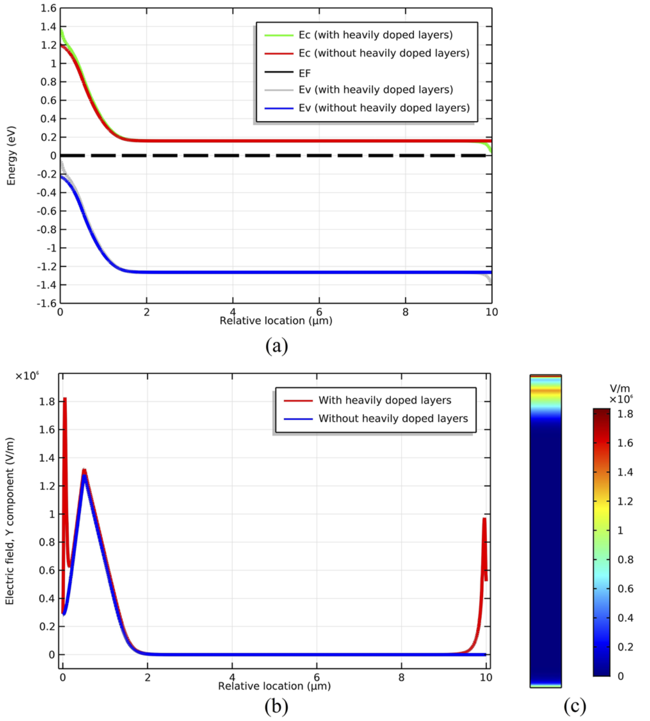

(a)

(b)

(c)

FIG. 3. (a) Energy diagram of the battery at thermodynamic equilibrium. (b) Y-component distribution of the electric field across the battery. (c) Y-component distribution of the electric field of the battery with heavily doped layers in 2D. The $H_{\text{p-GaAs}}$, $H_{\text{n-GaAs}}$, N_a, N_d, N_A, and N_D values are 0.5 μm, 9.5 μm, 1.58 $\times$ 10^{15} cm^{-3}, 1 $\times$ 10^{15} cm^{-3}, 1 $\times$ 10^{18} cm^{-3}, and 1 $\times$ 10^{17} cm^{-3}, respectively.

is close to the conductor band. The higher energy potential barrier contributes to the larger open-circuit voltage of the battery.

In our simulations, the Y-component (normal to the junction plane) of each physical quantity is significant. Thus, Fig. 3(b) shows the Y-component distribution of the electric field across the battery (the n-region pointing to the p-region is the positive direction of the electric field). It can be observed that for the battery without top and bottom heavily doped layers, the electric field is more intensive in the depletion region and reaches its maximum at the metallurgical junction as expected. The radiation-induced electron–hole pairs generated in this region can be collected by the drift mechanism and form the drift current. When the top and bottom layers are heavily doped, the drift fields will be formed between the p^+-GaAs (n^+-GaAs) and p-GaAs (n-GaAs) layers and increase the radiation-induced current by boosting the minority carrier transport in the battery. The Y-component distribution of the electric field of the battery is also shown in 2D [Fig. 3(c)], where the top and bottom layers are heavily doped.

Figure 4 shows the electron (n) and hole (p) concentration distributions across the battery without and with ^{63}Ni source irradiation. Due to the donor doping in the n-region and acceptor doping in the p-region, the electron and hole concentrations have a very large concentration gradient at the metallurgical junction. Meanwhile, the diffusion current driven by the concentration gradient and the drift current driven by the built-in electric field will remain in balance, and as a result, the total current density across the battery is 0. When the GaAs p–n junction is irradiated by the ^{63}Ni source, thousands of electron-hole pairs (excess electrons and holes) are generated, as shown by the red line in Fig. 4, and the minority electron concentration in the p-region and the minority hole concentration in the n-region will increase significantly. In the condition of short circuit, the balance between carrier diffusion and drift is broken. These radiation-induced excess electrons and holes will be separated by the built-in electric field, forming the electron drift current and hole drift current. The lower minority carrier concentration in the depletion region and near the cell surface can be explained as the carrier loss due to carrier drift, diffusion, and surface recombination.

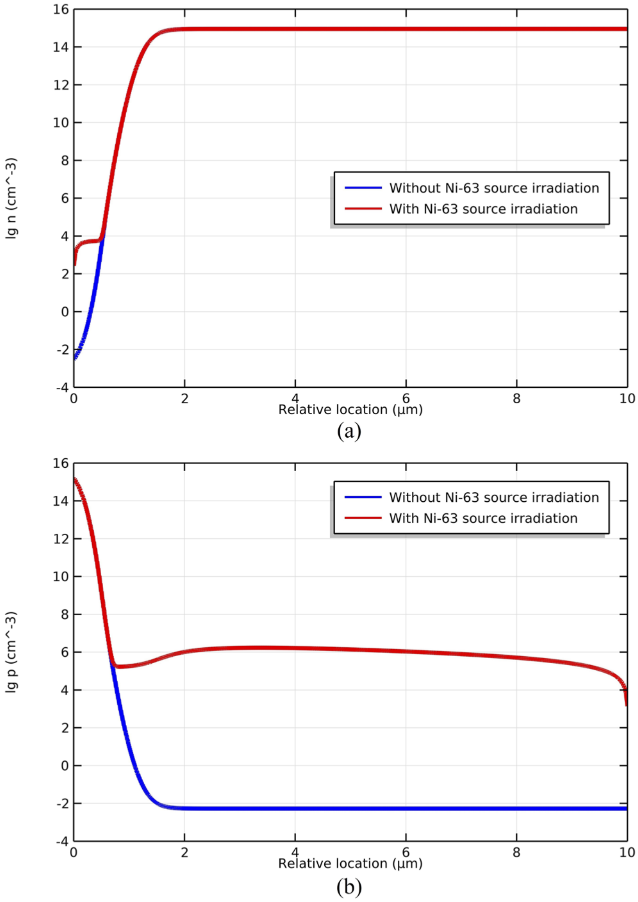

(a)

(b)

FIG. 4. (a) Electron concentration. (b) Hole concentration distribution across the battery (without heavily doped layers) without and with ^{63}Ni source irradiation. The $H_{\text{p-GaAs}}$, $H_{\text{n-GaAs}}$, N_a, and N_d values are 0.5 μm, 9.5 μm, 1.58 × 10^{15} cm^{-3}, and 1 × 10^{15} cm^{-3}, respectively.

B. Current density distribution and J–V characteristics

For a betavoltaic battery, in the condition of short circuit, the radiation-induced current consists of the electron current and the hole current, which also include the drift current and diffusion current components.[33] The Y-components of current densities of the battery (without heavily doped layers), which change following the relative location, are shown in Fig. 5 (the n-region pointing to the p-region is the positive direction of current density). It can be seen that in the range of ~0.1 to ~3.4 μm, both electrons and holes contribute to the total current and the short-circuit current density (J_{sc}) reaches 0.232 μA/cm^2. However, in the range of the top electrode to ~0.1 μm, only holes contribute to the total current. In the range of ~3.4 μm to the bottom electrode, only electrons contribute to the total current.

Figure 5(b) gives further details of electron drift and diffusion current density distributions. Due to the diffusion of electrons to the top electrode, the movement of electrons in the range of the top electrode to ~0.1 μm has no contribution, and as a result, the electron diffusion current density is negative. In the depletion region, the drift of electrons is dominant compared with the diffusion; thus, the positive total electron current density is achieved, which contributes to J_{sc}. In the n-region, the electrons are the majority carriers, and they move mainly in the drift mechanism. Both the electron drift current density and the electron diffusion current density resulting from the diffusion to the bottom electrode contribute to J_{sc}. It is worth noting that the flat band region (quasi-neutral region) actually has an electric field, but its intensity is very weak. The drift of the minority carriers is of low importance, while the drift of the majority carriers cannot be ignored.

The hole drift and diffusion current density distributions are shown in Fig. 5(c), which are similar to those of the electron. In the range of ~3.4 μm to the bottom electrode, the holes diffuse toward the bottom electrode and the hole diffusion current density is negative. However, as the holes approach the depletion region, the diffusion to the depletion region becomes dominant and the hole diffusion current density becomes positive. In the depletion region, the drift of holes is dominant compared with the diffusion, and the holes are constantly being swept into the p-region. In the p-region, the holes are the majority carriers, and they drift toward the top

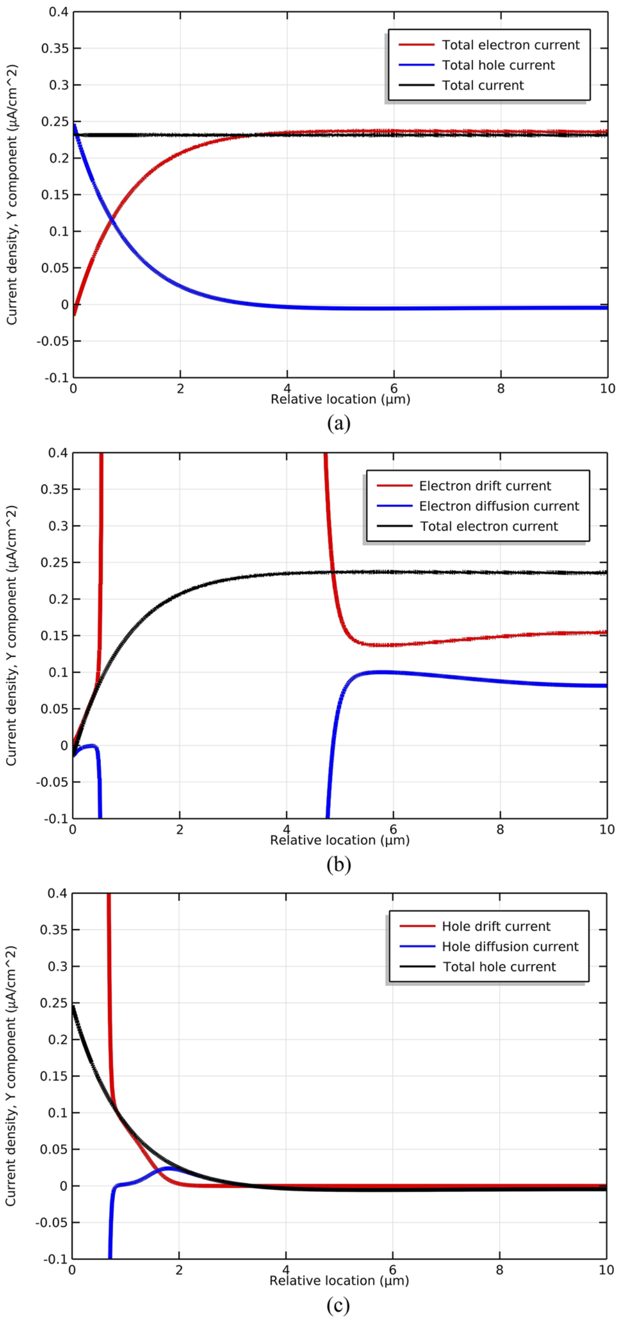

FIG. 5. (a) Y-component distributions of electron and hole current densities, (b) Y-component distributions of electron drift and diffusion current densities, and (c) Y-component distributions of hole drift and diffusion current densities in the short circuit condition. The $H_{\text{p-GaAs}}$, $H_{\text{n-GaAs}}$, N_a, and N_d values are 0.5 μm, 9.5 μm, 1.58 × 10^{15} cm^{-3}, and 1 × 10^{15} cm^{-3}, respectively.

electrode. The same as other current components mentioned above, they also contribute to J_{sc}.

So far, the Y-component distributions of current densities inside the battery in the condition of short circuit are obtained. Furthermore, by sweeping the forward voltage across the device and recording the terminal current, we can obtain the current density–voltage (J–V) and power density–voltage (P–V) characteristics of the betavoltaic battery. Figure 6 shows the J–V and P–V characteristics of the battery for two structures without and with heavily doped layers. For the battery without heavily doped layers, when the structure parameters are $H_{\text{p-GaAs}}$ = 0.5 μm, $H_{\text{n-GaAs}}$ = 9.5 μm, N_a = 1.58 × 10^{15} cm^{-3}, and N_d = 1 × 10^{15} cm^{-3} (the doping concentrations are also the optimized values, which will be presented later), the short-circuit current density, open-circuit voltage, and maximum output power density can reach 0.232 μA/cm^2, 0.44 V, and 0.072 μW/cm^2, respectively. When the top and bottom layers are heavily doped (N_A = 1 × 10^{18} cm^{-3} and N_D = 1 × 10^{17} cm^{-3}), the wider electric field region and higher energy potential barrier contribute to the larger short-circuit current density and higher open-circuit voltage. The increased drift current densities finally result in a larger short-circuit current density of 0.246 μA/cm^2, an open-circuit voltage of 0.50 V, and a maximum output power density of 0.086 μW/cm^2.

C. Parameter optimization of the batteries

Obviously, the thicknesses and doping concentrations of each region determine the energy band structure and electric field distribution inside a p–n junction and further affect the output performance of the battery. In order to optimize the structure parameters of the GaAs-based battery, the J–V characteristics, short-circuit current density (J_{sc}), open-circuit voltage (V_{oc}), and maximum output power density (P_m) are investigated with a variation of $H_{\text{p-GaAs}}$, N_a, and N_d. Figure 7(a) shows the J–V characteristics of the battery without heavily doped layers whose $H_{\text{p-GaAs}}$, $H_{\text{n-GaAs}}$, and N_d values are 0.5 μm, 9.5 μm, and 1 × 10^{15} cm^{-3}, respectively. It can be seen that as N_a increases, the current density changes significantly, to be specific, J_{sc} decreases, while V_{oc} increases. Figures 7(b) and 7(c) show the energy diagram and Y-component distribution of the electric field of the battery, respectively. The increase in the doping concentration N_a results in the decrease in the depletion region width; meanwhile, the depletion region is away from the surface of the

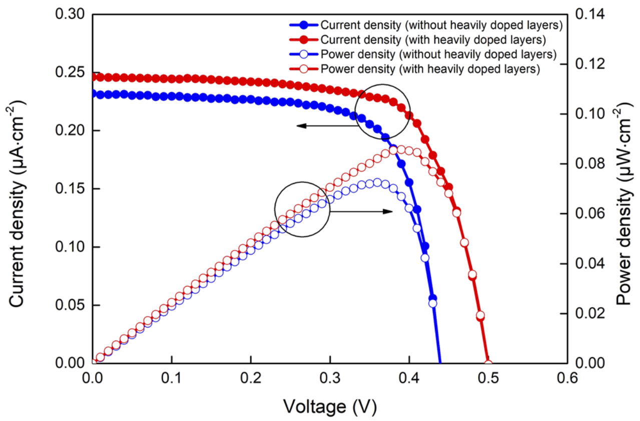

FIG. 6. J–V and P–V characteristics of the battery for two structures without and with heavily doped layers. The $H_{\text{p-GaAs}}$, $H_{\text{n-GaAs}}$, N_a, N_d, N_A, and N_D values are 0.5 μm, 9.5 μm, 1.58 × 10^{15} cm^{-3}, 1 × 10^{15} cm^{-3}, 1 × 10^{18} cm^{-3}, and 1 × 10^{17} cm^{-3}, respectively.

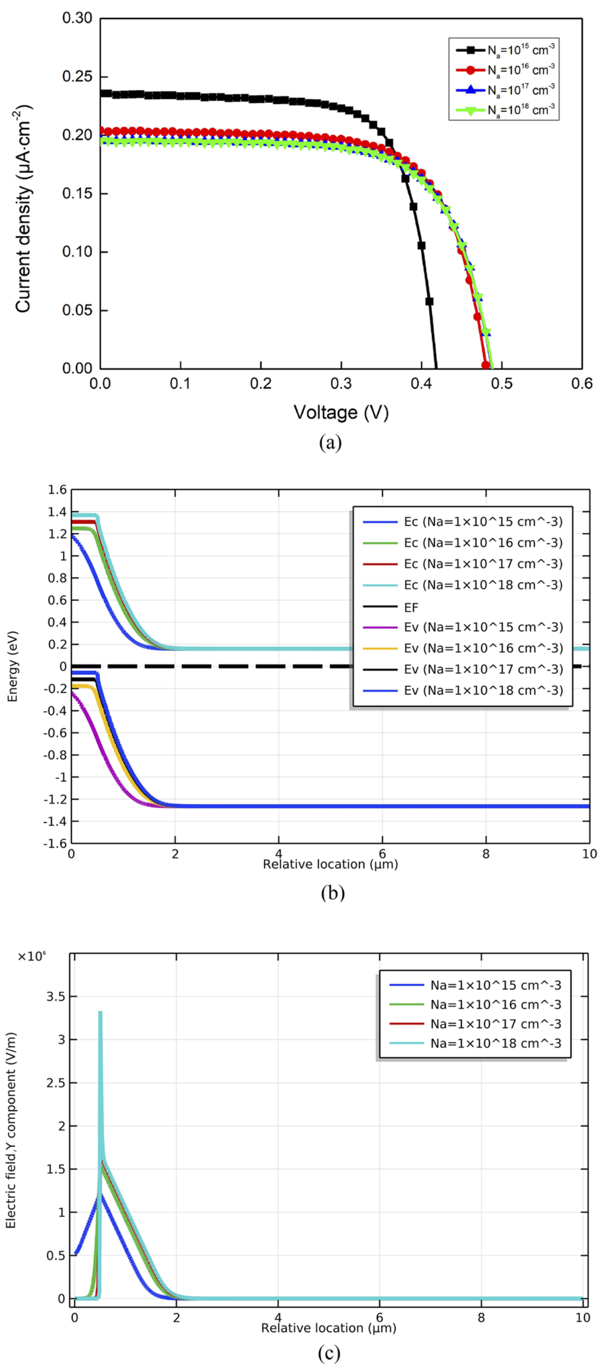

(a)

(b)

(c)

FIG. 7. (a) J–V characteristics, (b) energy diagram, and (c) Y-component distribution of the electric field of the battery without heavily doped layers. The $H_{\text{p-GaAs}}$, $H_{\text{n-GaAs}}$, and N_d values are 0.5 μm, 9.5 μm, and 1 × 10^{15} cm^{-3}, respectively.

p-region where the generation rate of electron-hole pairs is higher. Thus, the drift current densities decrease and the short-circuit current density J_{sc} decreases with increasing N_a. Conversely, the larger N_a value is beneficial to form the higher built-in potential barrier, which can enhance V_{oc}.

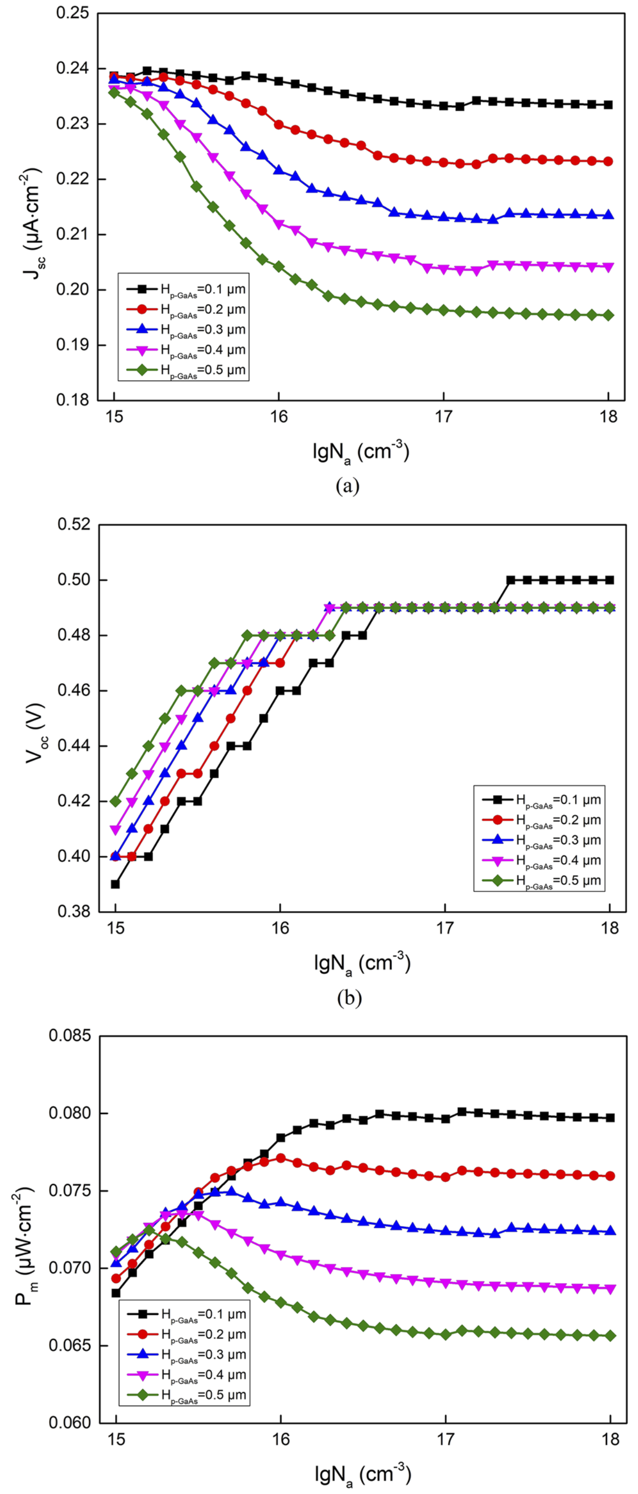

(a)

(b)

(c)

FIG. 8. Effects of $H_{\text{p-GaAs}}$ and N_a on the (a) J_{sc}, (b) V_{oc}, and (c) P_m values of the battery without heavily doped layers. When $H_{\text{p-GaAs}}$ is changed, $H_{\text{n-GaAs}}$ = 10 μm–$H_{\text{p-GaAs}}$, and when N_a is changed, N_d is fixed as 1 × 10^{15} cm^{-3}.

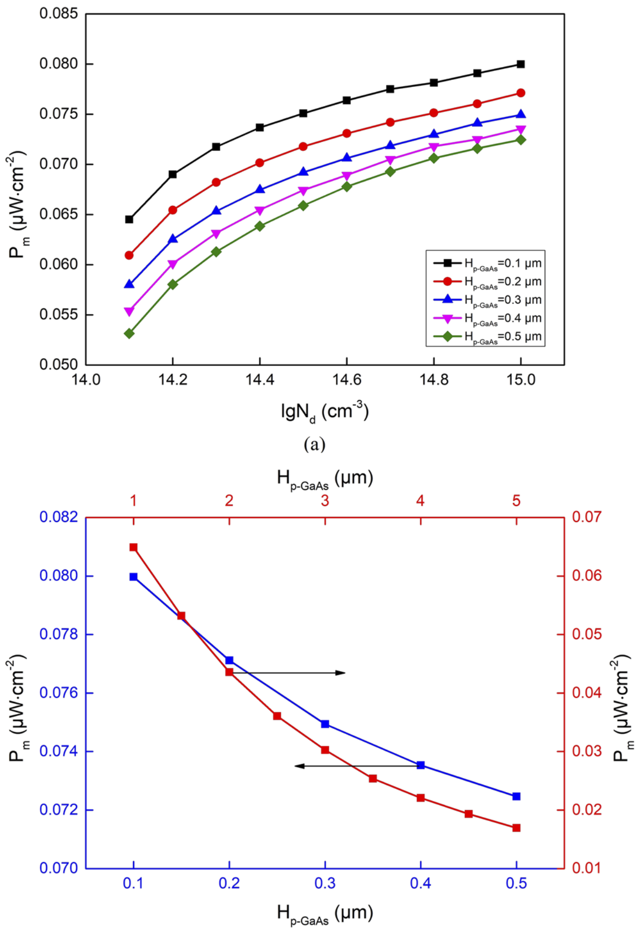

(a)

(b)

FIG. 9. (a) Effects of $H_{\text{p-GaAs}}$ and N_d on the P_m value of the battery without heavily doped layers. (b) P_m vs $H_{\text{p-GaAs}}$. When $H_{\text{p-GaAs}}$ is changed, $H_{\text{n-GaAs}}$ = 10 μm–$H_{\text{p-GaAs}}$, and when N_d is changed, N_a is fixed as the optimized doping concentration.

Furthermore, Figs. 8(a)–8(c) show the effects of $H_{\text{p-GaAs}}$ and N_a on J_{sc}, V_{oc}, and P_m. When $H_{\text{p-GaAs}}$ is changed, $H_{\text{n-GaAs}}$ = 10 μm–$H_{\text{p-GaAs}}$, and when N_a is changed, N_d is fixed as 1×10^{15} cm^{-3}. J_{sc} decreases with increasing $H_{\text{p-GaAs}}$, and this can be explained as larger $H_{\text{p-GaAs}}$, leading to the deeper junction, which has a lower collection efficiency of electron–hole pairs. As shown in Fig. 8(b), the open-circuit voltage (V_{oc}) increases with increasing N_a and shows the same trend for different $H_{\text{p-GaAs}}$ values. Ultimately, the maximum output power density (P_m) first increases with increasing N_a and then decreases. For the battery with an $H_{\text{p-GaAs}}$ value of 0.1 μm, the largest P_m value of 0.080 μW/cm^2 can be achieved when the doping concentrations are N_a = 3.98×10^{16} cm^{-3} and N_d = 1×10^{15} cm^{-3}. When the $H_{\text{p-GaAs}}$ value increases to 0.5 μm, the P_m value decreases to 0.072 μW/cm^2 with the optimized doping concentrations N_a = 1.58×10^{15} cm^{-3} and N_d = 1×10^{15} cm^{-3}.

Similarly, Fig. 9(a) shows the effects of $H_{\text{p-GaAs}}$ and N_d on P_m. When $H_{\text{p-GaAs}}$ is changed, $H_{\text{n-GaAs}}$ = 10 μm–$H_{\text{p-GaAs}}$, and when N_d is changed, N_a is fixed as the optimized doping concentration for different $H_{\text{p-GaAs}}$ values. It can be seen that P_m increases with increasing N_d and slows down at last. This indicates that larger N_d brings the higher built-in potential barrier and eventually contributes to higher V_{oc} and larger P_m. The decrease in P_m with increasing $H_{\text{p-GaAs}}$ can also be explained as larger $H_{\text{p-GaAs}}$, leading to the deeper junction, which is not conducive to the separation and collection of electron–hole pairs. When $H_{\text{p-GaAs}}$ is in the range of 0.1–5 μm and the doping concentrations (N_a and N_d) are optimized values, the relationship between P_m and $H_{\text{p-GaAs}}$ is shown in Fig. 9(b). To be specific, when $H_{\text{p-GaAs}}$ increases from 0.1 to 0.5 μm, P_m decreases from 0.080 to 0.072 μW/cm^2. When $H_{\text{p-GaAs}}$ increases to 5 μm, P_m is only 0.017 μW/cm^2.

For the battery with top and bottom heavily doped layers, the relationships among J_{sc}, V_{oc}, and P_m and $H_{\text{p-GaAs}}$, N_a, and N_d have also been investigated. The comparison of optimized output performances of the GaAs-based batteries is shown in Table II. For the sake of comparison, the optimized doping concentrations (N_a and N_d) of the battery for two structures without and with heavily doped layers are taken to be the same value. It can be seen that when the top and bottom heavily doped layers (N_A = 1×10^{18} cm^{-3} and $N_D = 1 \times 10^{17}$ cm^{-3}) are introduced, J_{sc} increases from 0.234 to 0.247 μA/cm^2, and P_m increases from 0.080 to 0.086 μW/cm^2.

IV. CONCLUSION

In summary, the performances of GaAs-based betavoltaic batteries with a p–n junction structure were predicted by our presented simulation model, and the carrier transport and collection characteristics were investigated. The Monte Carlo codes were used to calculate the electron-hole pair generation rate in the GaAs material under the irradiation of a ^{63}Ni source, and the finite element analysis software COMSOL Multiphysics was used to predict the battery performance. First, for the batteries without heavily doped layers, only in some areas, both the electron and hole drift current densities contribute to J_{sc}. This depends on the structure parameters. The J_{sc}, V_{oc}, P_m, and η values of the batteries are significantly affected

TABLE II. Comparison of optimized output performances of the GaAs-based batteries.

$H_{\text{p-GaAs}}$ (μm)	$H_{\text{n-GaAs}}$ (μm)	N_a (cm^{-3})	N_d (cm^{-3})	N_A (cm^{-3})	N_D (cm^{-3})	J_{sc} (μA/cm^2)	V_{oc} (V)	P_m (μW/cm^2)	η (%)
0.1	9.9	3.98×10^{16}	1×10^{15}	⋯	⋯	0.234	0.49	0.080	1.55
0.2	9.8	1.00×10^{16}	1×10^{15}	⋯	⋯	0.230	0.47	0.077	1.50
0.3	9.7	5.01×10^{15}	1×10^{15}	⋯	⋯	0.229	0.46	0.075	1.46
0.4	9.6	2.51×10^{15}	1×10^{15}	⋯	⋯	0.230	0.45	0.074	1.44
0.5	9.5	1.58×10^{15}	1×10^{15}	⋯	⋯	0.232	0.44	0.072	1.40
0.1	9.9	3.98×10^{16}	1×10^{15}	1×10^{18}	1×10^{17}	0.247	0.50	0.086	1.67

by $H_{\text{p-GaAs}}$, $H_{\text{n-GaAs}}$, N_a, and N_d. The lower N_a value is beneficial to obtain a wider depletion region, and furthermore, a larger J_{sc} value can be achieved. However, the higher N_a value contributes to the higher built-in potential barrier, which can enhance V_{oc}. Thus, the largest P_m value of 0.080 μW/cm^2 can be achieved when the thicknesses and doping concentrations of each region are $H_{\text{p-GaAs}} = 0.1$ μm, $H_{\text{n-GaAs}} = 9.9$ μm, $N_a = 3.98 \times 10^{16}$ cm^{-3}, and $N_d = 1 \times 10^{15}$ cm^{-3}. The related J_{sc}, V_{oc}, and η values are 0.234 μA/cm^2, 0.49 V, and 1.55%, respectively. Second, when the top and bottom layers are heavily doped ($N_A = 1 \times 10^{18}$ cm^{-3} and $N_D = 1 \times 10^{17}$ cm^{-3}), the drift fields are formed and the higher energy potential barrier enhances the battery performance. The optimized J_{sc}, V_{oc}, P_m, and η values are 0.247 μA/cm^2, 0.50 V, 0.086 μW/cm^2, and 1.67%, respectively. Although the GaAs-based betavoltaic batteries were investigated in this study, our simulation model can be extended to the betavoltaic batteries with other semiconductors and isotopes for the optimization and fabrication. Finally, we will fabricate the proposed GaAs-based betavoltaic batteries using the metalorganic chemical vapor deposition (MOCVD) and validate the simulation model in the future work.

ACKNOWLEDGMENTS

This work was supported by the National Natural Science Foundation of China (Grant Nos. 11075064 and U1867210) and the National Major Scientific Instruments and Equipment Development Projects (Grant No. 2012YQ240121).

AUTHOR DECLARATIONS

Conflict of Interest

The authors have no conflicts to disclose.

DATA AVAILABILITY

The data that support the findings of this study are available from the corresponding author upon reasonable request.

REFERENCES

[1] M. A. Prelas, C. L. Weaver, M. L. Watermann, E. D. Lukosi, R. J. Schott, and D. A. Wisniewski, "A review of nuclear batteries," Prog. Nucl. Energy **75**, 117–148 (2014).

[2] L. C. Olsen, P. Cabauy, and B. J. Elkind, "Betavoltaic power sources," Phys. Today **65**(12), 35–38 (2012).

[3] M. G. Spencer and T. Alam, "High power direct energy conversion by nuclear batteries," Appl. Phys. Rev. **6**, 031305 (2019).

[4] S. Butera, G. Lioliou, and A. M. Barnett, "Temperature effects on gallium arsenide ^{63}Ni betavoltaic cell," Appl. Radiat. Isot. **125**, 42–47 (2017).

[5] M. A. Prelas, M. Boraas, F. D. Aguilar, J. D. Seelig, M. T. Tchouaso, and D. Wisniewski, *Nuclear Batteries and Radioisotopes*, Lecture Notes in Energy Vol. 56 (Springer Press, Switzerland, 2016).

[6] Y.-p. Liu, X.-b. Tang, Z.-h. Xu, L. Hong, H. Wang, M. Liu, and D. Chen, "Influences of planar source thickness on betavoltaics with different semiconductors," J. Radioanal. Nucl. Chem. **304**, 517–525 (2015).

[7] H. Wang, X.-b. Tang, Y.-P. Liu, Z.-H. Xu, M. Liu, and D. Chen, "Temperature effect on betavoltaic microbatteries based on Si and GaAs under ^{63}Ni and ^{147}Pm irradiation," Nucl. Instrum. Methods Phys. Res., Sect. B **359**, 36–43 (2015).

[8] Y.-M. Liu, J.-B. Lu, X.-Y. Li, X. Xu, R. He, and H.-D. Wang, "A 4H-SiC betavoltaic battery based on a ^{63}Ni source," Nucl. Sci. Tech. **29**, 168 (2018).

[9] M. Lu, G.-g. Zhang, K. Fu, G.-h. Yu, D. Su, and J.-f. Hu, "Gallium nitride Schottky betavoltaic nuclear batteries," Energy Convers. Manage. **52**(4), 1955–1958 (2011).

[10] D.-Y. Qiao, X.-J. Chen, Y. Ren, and W.-Z. Yuan, "A micro nuclear battery based on SiC Schottky barrier diode," J. Microelectromech. Syst. **20**(3), 685–690 (2011).

[11] F. Rahmani and H. Khosravinia, "Optimization of silicon parameters as a betavoltaic battery: Comparison of Si p-n and Ni/Si Schottky barrier," Radiat. Phys. Chem. **125**, 205–212 (2016).

[12] M. Wu, S. Wang, Y. Ou, and W. Wang, "Optimization design of betavoltaic battery based on titanium tritide and silicon using Monte Carlo code," Appl. Radiat. Isot. **142**, 22–27 (2018).

[13] H. San, S. Yao, X. Wang, Z. Cheng, and X. Chen, "Design and simulation of GaN based Schottky betavoltaic nuclear micro-battery," Appl. Radiat. Isot. **80**, 17–22 (2013).

[14] H. Y. Chen, L. Jiang, and D. R. Li, "Measurement of beta particles induced electron-hole pairs recombination in depletion region of GaAs PN junction," Chin. Phys. Lett. **28**(5), 058101 (2011).

[15] H. Y. Chen, L. Jiang, and X. Y. Chen, "Design optimization of GaAs betavoltaic batteries," J. Phys. D: Appl. Phys. **44**, 215303 (2011).

[16] Z. Cheng, X. Chen, H. San, Z. Feng, and B. Liu, "A high open-circuit voltage gallium nitride betavoltaic microbattery," J. Micromech. Microeng. **22** 074011 (2012).

[17] A. A. Svintsov, A. A. Krasnov, M. A. Polikarpov, A. Y. Polyakov, and E. B. Yakimov, "Betavoltaic battery performance: Comparison of modeling and experiment," Appl. Radiat. Isot. **137**, 184–189 (2018).

[18] G. N. Yakubova, *Nuclear Batteries with Tritium and Promethium-147 Radioactive Sources* (University of Illinois, Urbana, 2010).

[19] G. R. Ghasemi Nejad, F. Rahmani, and G. R. Abaeiani, "Design and optimization of beta-cell temperature sensor based on ^{63}Ni–Si," Appl. Radiat. Isot. **86**, 46–51 (2014).

[20] C. A. Klein, "Bandgap dependence and related features of radiation ionization energies in semiconductors," J. Appl. Phys. **39**, 2029–2038 (1968).

[21] K. Zhang, P. Pathak, F. Cerrina, and Z. Q. Ma, "Performance prediction of nuclear micro power sources based on beta emitters," ECS Trans. **19**, 45 (2009).

[22] G. Gui, K. Zhang, J. P. Blanchard, and Z. Ma, "Prediction of 4H–SiC betavoltaic micro battery characteristics based on practical Ni-63 sources," Appl. Radiat. Isot. **107**, 272–277 (2016).

[23] Y. J. Yoon, J. S. Lee, I. M. Kang, J. H. Lee, and D. S. Kim, "Design optimization of GaN diode with p-GaN multi-well structure for high-efficiency betavoltaic cell," Nucl. Eng. Technol. **53**(4), 1284–1288 (2020).

[24] Y. J. Yoon, J. S. Lee, I. M. Kang, J. H. Lee, and D. S. Kim, "Design and analysis of gallium nitride-based p-i-n diode structure for betavoltaic cell with enhanced output power density," Micromachines **11**, 1100 (2020).

[25] Y. J. Yoon, J. S. Lee, I. M. Kang, J. H. Lee, and D. S. Kim, "Design and optimization of GaN-based betavoltaic cell for enhanced output power density," Int. J. Energy Res. **45**, 799–806 (2021).

[26] D. L. Wagner, D. R. Novog, and R. R. Lapierre, "Design and optimization of nanowire betavoltaic generators," J. Appl. Phys. **127**, 244303 (2020).

[27] D. L. Wagner, D. R. Novog, and R. R. Lapierre, "Genetic algorithm optimization of core-shell nanowire betavoltaic generators," Nanotechnology **31**, 455403 (2020).

[28] M. Sotoodeh, A. H. Khalid, and A. A. Rezazadeh, "Empirical low-field mobility model for III–V compounds applicable in device simulation codes," J. Appl. Phys. **87**, 2890–2900 (2000).

[29] M. S. Lundstrom, M. E. Klausmeier-Brown, M. R. Melloch, R. K. Ahrenkiel, and B. M. Keyes, "Device-related material properties of heavily doped gallium arsenide," Solid-State Electron. **33**(6), 693–704 (1990).

[30] X. Li, N. P. Hylton, V. Giannini, K.-H. Lee, N. J. Ekins-Daukes, and S. A. Maier, "Multi-dimensional modeling of solar cells with electromagnetic and carrier transport calculations," Prog. Photovoltaics **21**, 109–120 (2013).

[31] N. Bednar, N. Severino, and N. Adamovic, "Optical simulation of light management in CIGS thin-film solar cells using finite element method," Appl. Sci. **5**, 1735–1744 (2015).

[32] D. A. Neamen, *Semiconductor Physics and Devices: Basic Principles*, 4th ed. (Publishing House of Electronics Industry; McGraw-Hill Education, Xi'an, 2017), pp. 248–630.

[33] S. Fonash, *Solar Cell Device Physics* (Elsevier, Inc., New York, 2016), pp. 102–110.